Comparative analysis of gas atomised and recycled 316L stainless steel powders for Binder Jetting

M. Mariani, K. Salaheldin, A. Grande, N. Lecis

In our work, we investigate the suitability of a 316L stainless steel powder from scrap metal recycling for binder jetting and the results are compared to those obtained for a gas atomised feedstock. First, the main morphological features of the particles, in particular sphericity and size distribution, are measured by static image granulometry and scanning electron microscopy. Then, the dispensing rate and the printer deposition parameters are optimised to obtain a smooth and homogeneous powder bed. After printing, the building box is cured at 180 °C to consolidate the green components, whose density and geometrical accuracy are determined by caliper measurement. Finally, the microstructural and mechanical properties of the vacuum sintered specimens are studied. Phase composition is determined by x-ray diffraction and microscopy, with specific attention to δ-ferrite formation at the grain boundary. Hardness is evaluated by Vickers micro-indentation and compared to typical properties of 316L by conventional manufacturing.

KEYWORDS: BINDER JETTING; 316L STAINLESS STEEL; SINTERING; AUSTENITE; FERRITE

INTRODUCTION

Additive manufacturing (AM) comprises a long series of techniques suitable to produce components with a high degree of geometrical complexity. Among these processes, metal binder jetting (BJT) is progressively gathering the interest of the academic and industrial sectors due to a series of advantages. This technique is based on a first shaping phase, during which a liquid bonding agent is deposited on a powder bed in a layerwise manner according to the specimen design, followed by a series of post-processing treatments. In detail, curing at low temperature induces the polymerisation of the liquid species to consolidate the green bodies, debinding removes any trace of organic material and sintering promotes the removal of porosity and the densification of the components. If needed, additional treatments as hot isostatic pressing, slurry infiltration, annealing, and others, may be performed to modify or improve the performances of the printed parts.

The main advantage of BJT lies in the possibility of obtaining a finer control on the microstructural properties, thus on mechanical ones too, with respect to powder bed fusion techniques due to proper tuning of the heat treatments, as occurs in conventional powder metallurgy techniques

Marco Mariani, Karim Salaheldin, Nora Lecis*
Dipartimento di Meccanica, Politecnico di Milano

Antonio Maria Grande
Dipartimento di Scienze e Tecnologie Aerospaziali, Politecnico di Milano

*nora.lecis@polimi.it

(e.g. powder forging, metal injection moulding...) (1). Secondarily, geometrical limitations to the designs are minimal, namely only closed cavities, differently from other direct and indirect AM techniques that requires supports for overhangs, limited step angles and so on (2). The main drawback consists in the strong dependence of the sintered components features on the feedstock material employed during printing. Indeed, the powder influences the mechanisms of formation of the components during the initial shaping phase and densification at later stages. Powder morphology (shape and size distribution), chemical composition and surface properties are responsible for the feedstock flowability, which is the main contribution to the proper packing of the particles in the building box, thus to the green body density (3,4). Maximising the green density facilitates the sintering process, however other phenomena must be kept into account to understand densification mechanisms. Indeed, necking and shrinkage rates are dependent not only on coordination numbers of the particles, but also on the specific composition of the feedstock that affects phase transformations, diffusion mechanisms and liquid phase formation (5). Exceeding the solidus temperature has become a common trend in metal BJT because liquid sintering allows to rapidly fill residual porosity, however a fine control on the elemental composition is needed (6–8) and possible shape distortions should be accounted for.

In this study, two feedstocks of 316L stainless steel are employed to observe the effects of chemical composition variations on each step of production by BJT. A comparative analysis of the microstructural properties is performed and correlated to densification mechanisms according to phase transformation modelling.

MATERIALS AND METHODS

Samples production

Two 316L stainless steel feedstocks are mentioned in the study:

"F") A spherical powder from f3nice Srl obtained from atomisation of recycled scrap steel;

"S") A spherical powder from Sandvik AB produced from gas atomisation of molten metal with controlled chemical composition.

Powder F properties and performances are compared to powder S, which has been extensively studied and described in literature.

The components were manufactured with an Innovent+ printer from ExOne with deposition and spreading parameters optimised according to the flowability of each feedstock, a layer thickness (LT) of 50 μm and a binder saturation (BS) of 55% and 70%. Three sizes of parallelepiped specimens were produced: small (8 x 6 x 4 mm^3), medium (16 x 12 x 18 mm^3) and large (24 x 18 x 12 mm^3). The parts underwent the following thermal treatments, optimised in previous studies (6,9,10):

1. Curing at 180 °C for 6 hours in natural air convection furnace YAMATO DX 412C to polymerise the polyethylene glycol (PEG) precursors contained in the binder and consolidate the green bodies;
2. Debinding at 470 °C for 4 hours in Ar in a tubular furnace CARBOLITE 12/75/700 to remove almost entirely the organic traces without oxidating the materials;
3. Sintering at 1360 °C for 3 hours in a vacuum (10^{-1} mbar) furnace HTS HT-S1 LPC to densify the components.

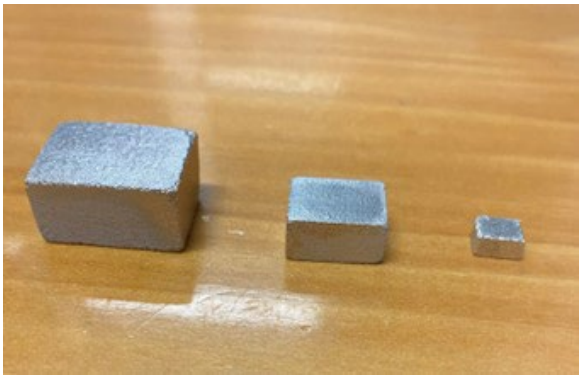

Fig.1 - Large, medium and small sintered components obtained from powder F3nice (F) / Componente sinterizzato grande, medio e piccolo ottenuto da polvere F3nice (F).

Samples characterisation

First, the powders were characterised with a static image optical granulometer Malvern Morphology 4 and x-ray diffractometer (XRD) SmartLab SE Rigaku. The chemical composition is determined by inductively coupled plasma (ICP) atomic emission spectroscopy on pristine particles.
Then, the printed samples were analysed geometrically to assess their accuracy and density at the green and brown stages. Archimedes' density was measured only for the sintered bodies. In both cases, the theorical density was set at 7.83 g cm^{-3}, as calculated from thermodynamic modelling based on the specific chemical composition of powder F. Microstructural features, such as grains, pores and secondary phases, were studied by field emission scanning electron microscopy (FE-SEM) equipped with energy dispersive x-ray (EDX) detector (Zeiss Sigma 500) and optical microscopy (Nikon Eclipse LV250NL), combined with XRD to determine the phase composition.
Vickers hardness was evaluated at the core and superficial (2 mm from the surface) regions of large samples with an applied load of 300 gf for 15 s.

Phase transformation modelling

Phase transformation mechanisms occurring during sintering are studied by CALPHAD-based simulations performed by ThermoCalc AB software under the hypothesis of thermodynamic equilibrium. One axis phase diagrams were modelled for the two powder based on their chemical compositions, as measured by ICP. Phase diagrams accounting for Cr, Ni and Mo mass percentages variations were calculated starting from the aforementioned chemical compositions with an addition of 0.1% in mass of C to simulate carbon-pickup from organic residue.

RESULTS AND DISCUSSION

Pre-sintering characterisation

As can be seen from Fig. 2A, both feedstocks display an optimal circularity, which should grant a decent flowability and packing behaviour during the printing phase, while the size distribution curves (Fig. 2B) underline a minimal distinction. Indeed, the F powder features an ultrafine fraction (500 nm – 1.5 μm) that is absent in the other feedstock. From the XRD spectra in Fig. 3, it appears that powder F contains a larger fraction of ferrite which could be either due to the specific chemical composition and to the atomisation process parameters as heating and cooling rates. According to the elemental compositions in Tab. 1, the concentration of ferritising elements in the two feedstocks is comparable, while that of austenitising ones is more relevant (the sharp increase of Ni, compensates for the decrease of Mn) in powder F. From simulation of phase formation diagrams at the equilibrium (Fig. 4), a higher content of ferrite should be expected in powder S, meaning that the thermal cycles applied to the powders during production are determinant on phases formation.

Tab.1 - Elemental composition measured by ICP of f3nice (F) e Sandvik (S) powders, and compositional ranges according to the AISI standard / Composizione elementale misurata tramite ICP delle polveri f3nice (F) e Sandvik (S), e intervalli di composizione secondo lo standard AISI.

	C	Si	Cr	Ni	Mo	Mn	Fe	O
F3nice	0.03	0.36	18.00	13.9	2.63	1.13	63.38	0.05
Sandvik	0.03	0.58	18.28	10.9	2.12	2.19	65.73	0.21
Sandvik	0.03	0.58	18.28	10.9	2.12	2.19	65.73	

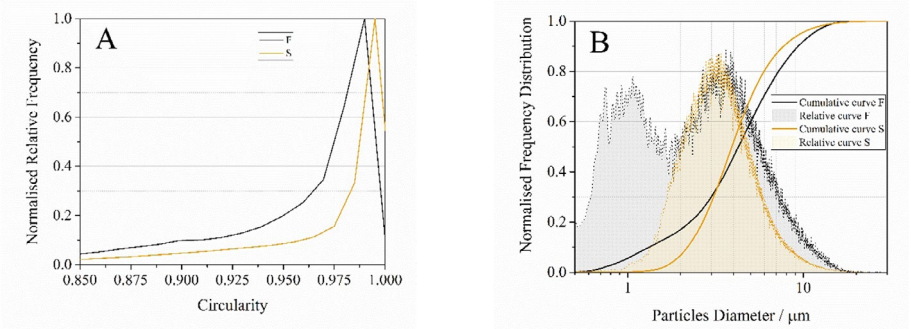

Fig. 2 - A) Circularity and B) size distribution curves of the f3nice (F) and Sandvik (S) feedstocks / Curve di distribuzione della A) circolarità e B) dimensione delle polveri f3nice(F) e Sandvik (S).

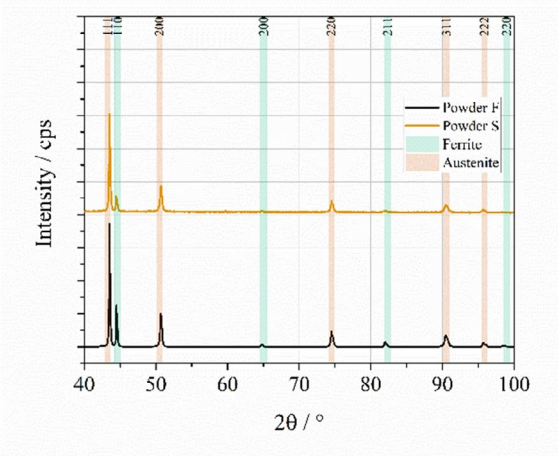

Fig.3 - Diffraction spectra of f3nice (F) e Sandvik (S) powders with diffraction patterns of ferrite and austenite / Spettri di diffrazione delle polveri f3nice (F) e Sandvik (S) con i pattern di diffrazione della ferrite e dell'austenite.

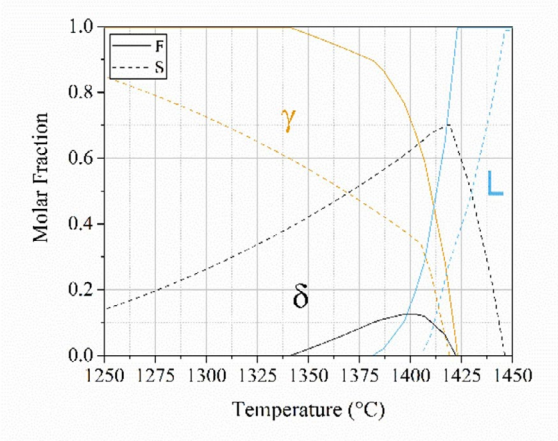

Fig.4 - Phase diagrams calculated from the chemical composition of f3nice (F – straight line) and Sandvik (S – dashed line) powders / Diagrammi di fase calcolati a partire dalla composizione chimica della polvere f3nice (F – linea continua) e Sandvik (S – linea tratteggiata).

The measure of the relative density values of the green and brown components in Tab. 2 reveals that:

- Small components have a lower density, likely due to a more relevant effect of small surface defects on the estimate of the pieces volume (also highlighted by the larger values standard deviations).
- BS70% components feature a higher density both at the green stage (due to the larger content of binder) and at the brown stage (mainly due to improved particles retention during handling before debinding).
- Weight loss from debinding is minimal as expected from the low amount of polymer in the binder (6).

The relative densities are lower than those obtained from powder S, whose average values were above 55% for both conditions after curing (6), thus the packing behaviour of powder F is poorer. Considering that the phase compositions and the circularity of the particles are similar in the two cases, the lower density should be ascribed to the size distributions. As seen in Fig. 2B, powder F features an additional ultrafine fraction that may responsible for a lower flowability of the particles due to rising of electrostatic interactions and residual humidity-induced capillarity among particles with reduced diameter (11). From literature, multimodal distributions should improve particles packing, but the ratio of diameters and volume fractions of the fine and coarse fractions should be properly optimised and all particles need a sufficient flowability, which is not occurring in this case (12).

Tab.2 - Relative densities of green, brown and sintered components obtained from f3nice (F) powders with binder saturation of 55% and 70% / Densità relative dei component verdi, decerati e sinterizzati ottenuti dalle polveri f3nice (F) con una saturazione di legante pari al 55% e al 70%.

	Green relative density [%]		Brown relative density [%]		Sintered relative density [%]	
Binder saturation	55%	70%	55%	70%	55%	70%
Small	48.3 ± 1.3	49.1 ± 0.7	44.9 ±1.0	47.1 ± 0.4	93.3 ± 0.8	93.1 ± 1.0
Medium	50.2 ± 0.4	50.6 ± 0.4	48.0 ± 0.7	49.8 ± 0.1	90.5 ± 0.9	88.8 ± 0.7
Large	50.8 ± 0.6	50.7 ± 0.7	49.6 ± 0.4	49.6 ± 0.2	90.3 ± 1.1	86.4 ± 0.9
Total	49.3 ± 1.3	49.9 ± 1.0	47.0 ± 2.2	48.5 ± 1.3	91.7 ± 1.7	89.9 ± 3.0

Post-sintering characterisation

The sintering treatment succeeded in reaching the final stage, where residual porosity is closed and rounded, as can be seen from Fig. 5. This is to be expected considering that the sintered relative densities (from Archimedes' method) are close or above 90% depending on the size and binder saturation of the samples (see Tab. 2). As expected, smaller samples densify faster because internal thermal gradients are minimised and pores diffusion toward the surface is shortened (13), while large components tend to retain residual porosity in the core regions (14,15). This inhomogeneity in pores distribution is confirmed by image analysis on micrographs from large BS55% samples, indeed porosity fractions of 8.3 ± 2.5% and 10.7 ± 1.9% were detected at the superficial and core areas, and by microhardness measurements with values of 90.1 ± 13 HV and 107.5 ± 16 HV at the centre and side of the samples, respectively.

The detrimental effect of larger binder saturation is confirmed and enhanced in the case of medium and large parts. Indeed, densification rates are equal to +44.7% and + 41.4% for BS55% and BS70% respectively. Although specimens integrity and density may be improved at the green and brown stages, the excess porosity left after polymer burnout negatively affects densification because it tends to be larger and concentrated at the layer interfaces where binder is deposited (16).

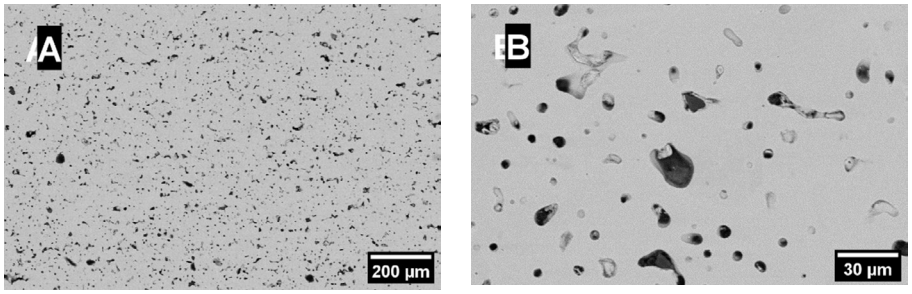

Fig.5 - Micrographies of the core region of samples obtained with BS55% from different magnifications / Micrografie della regione centrale dei campioni ottenuti con BS55% a diversi ingrandimenti.

Microstructural analysis

The comparative analysis of the microstructures obtained from the two feedstocks reveals that both the residual porosity amounts, and the phase distributions are different. Indeed, specimens F were less densified (98.3 ± 0.1% vs 91.7 ± 1.7% relative densities of BS55% for powder S and F, respectively) and they do not feature the marked presence of δ-ferrite at the grain boundaries that was evident in specimens S. Ferrite could be found only in specific spots and within limited regions, as can be seen in Fig. 6.

The lower green density hinders densification mechanisms, however the different phase distribution suggests that also other aspects should be considered. First, distinct chemical compositions of the feedstocks affect the stability range of austenite at high temperatures

and the formation of ferrite and liquid phases. In addition, elements distributions within particles are not uniform: Cr and Mo tends to segregate at the grain boundaries due to self-diffusion mechanisms, thus enriching the core of the particles with austenitising elements (17). Finally, carbon pickup from binder residue on particles surfaces might occur, as debinding in argon is incomplete (6,18).

Phase diagrams obtained from equilibrium simulations (Fig. 4) show that austenitising elements expand the stability window of the γ phase and reduce that of δ, thus increasing the temperature of formation of the ferrite and slightly reducing that of the liquid phase, even though it still stands above 1380 °C. At 1360 °C, powder F features about 5 mol.% of δ-ferrite concentrated at the grain boundary where Cr tends to segregate, while in powder S it should amount to about 45 mol.% as consequence of the lower amount of Ni in the composition. The study of phase diagrams with varying concentrations of Cr, Ni and Mo in Fig. 7 demonstrate that local fluctuations in the concentration of alloying elements can be responsible for the reduction of the solidus line below the sintering temperature. By considering the variations of compositions (enrichment of Cr and Mo, and reduction of Ni) at the grain boundaries, as deducted from the EDX measurements in Tab. 3, it can be observed that Cr and Mo increase to 24% and 4% in mass, respectively, can lead to liquid phase formation well below 1360 °C. Ferritising elements (Cr, Mo and C) effectively reduce the solidus line, thus favouring the formation of liquid phase prior to complete melting and increasing the pore filling effect required for densification (19).

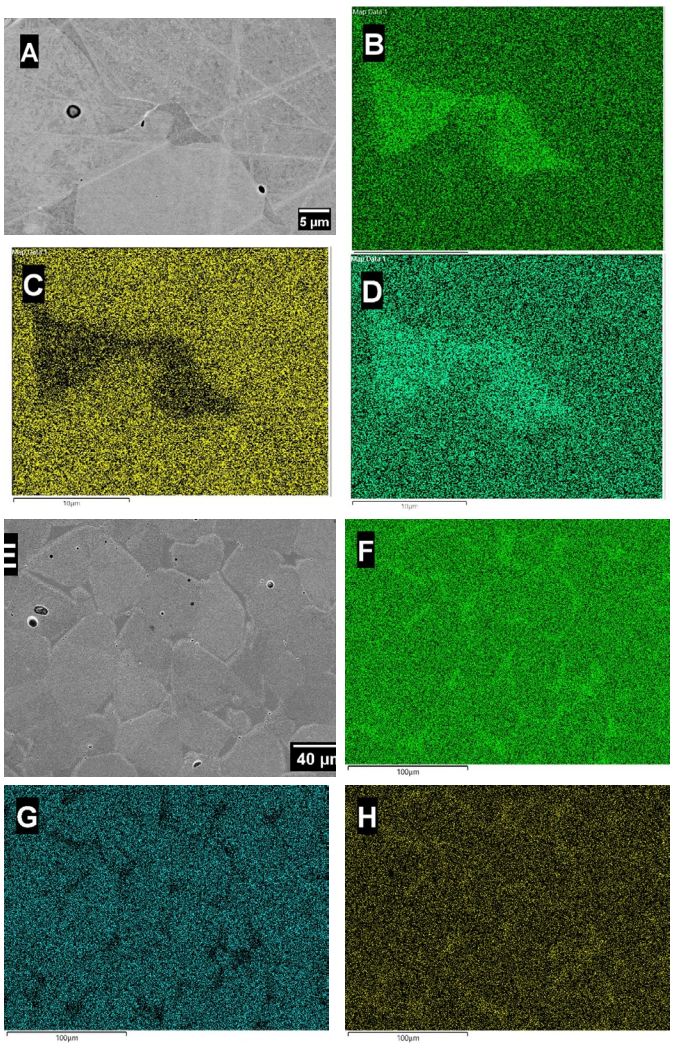

Fig.6 - EDS maps of samples BS55% from f3nice (A,B,C,D) and Sandvik (E,F,G,H) powders of the concentration of Cr (B,F), Ni (C,G) and Mo (D,H) in presence of ferrite at the grain boundary / Mappe EDX dei campioni BS55% da polvere f3nice (A,B,C,D) e Sandvik (E,F,G,H) della concentrazione di Cr (B,F), Ni (C,G) e Mo (D,H) in presenza di ferrite a bordo grano

Tab.3 - Elemental composition (mass percentages) measured by EDX of the phases γ e δ in samples BS55% from f3nice (F) e Sandvik (S) powders / Composizione elementale (in massa percentuale) misurata tramite EDX della fase γ e δ nei campioni BS55% da polveri f3nice (F) e Sandvik (S).

Powder	Phase	Si	Cr	Ni	Mo	Mn	Fe
F3nice	γ	0.43	16.93	11.83	2.27	1.43	66.87
	δ	0.54	23.14	5.30	4.93	1.13	64.72
Sandvik	γ	0.48	17.39	10.83	1.70	1.70	67.89
	δ	0.53	24.01	5.33	3.83	1.56	64.61

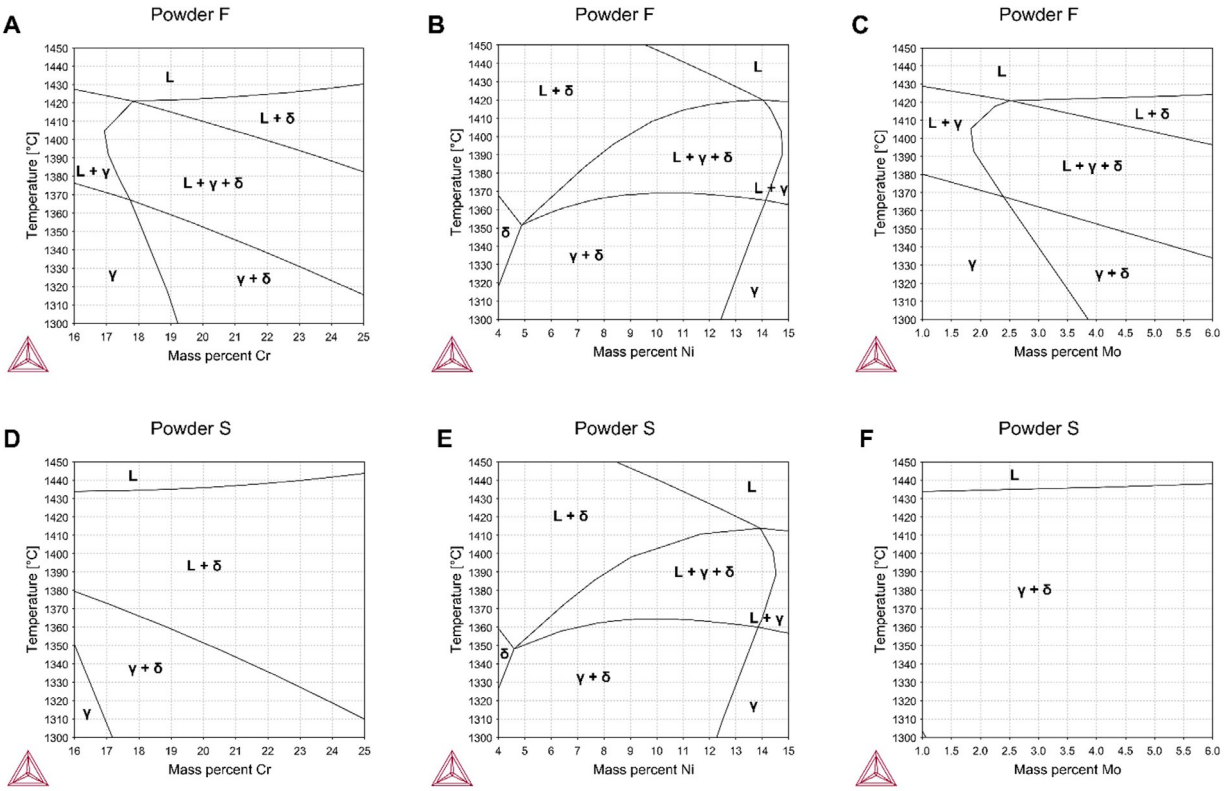

Fig.7 - Phase diagrams calculated from the chemical composition of the f3nice-F (A,B,C) and Sandvik-S (D,E,F) powders by varying the mass percentages of Cr (A,D), Ni (B,E) and Mo (C,F) / Diagrammi di fase calcolati dalle composizioni chimiche di A,B,C) polveri f3nice (F) e D,E,F) Sandvik (S) al variare della massa percentuale di Cr (A,D), Ni (B,E) e Mo (C,F).

CONCLUSIONS

This work analyses the effects of powder features and binder jetting procedures (printing phase and thermal treatments) on the microstructural properties of the final components. The employment of particles of the same nominal material (stainless steel 316L) allows to underline which are the main mechanisms of densification and how the effective chemical composition of the feedstocks affects the phase transformation mechanisms.

In particular, it was observed that the larger concentration of austenitising elements stabilises the γ phase at the sintering temperature, preventing the formation of large fractions of liquid phase, thus densification by supersolidus liquid phase sintering (SLPS). As a consequence, residual porosity at the grain boundaries is increased and grain boundaries decoration by δ-ferrite is minimised.

In conclusion, materials design is fundamental to determine the effective properties of the 3D printed components and

specific attention should be placed on assessing the effect of alloying elements on sintering mechanisms and phase transformations.

ACKNOWLEDGEMENTS

The authors acknowledge the support provided by f3nice Srl for the powder supply. The authors would like to acknowledge also the "Functional Sintered Materials (Funtasma)" Interdepartmental Laboratory of Politecnico di Milano, where this research activity was developed and the support by the Italian Ministry for Education, University and Research through the project Department of Excellence LIS4.0 (Integrated Laboratory for Lightweight e Smart Structures).

BIBLIOGRAFIA

[1] Kumar P, Jayaraj R, Suryawanshi J, Satwik UR, McKinnell J, Ramamurty U. Fatigue strength of additively manufactured 316L austenitic stainless steel. Acta Mater. 2020 Oct 15;199:225–39.

[2] Zago M, Lecis NFM, Vedani M, Cristofolini I. Dimensional and geometrical precision of parts produced by binder jetting process as affected by the anisotropic shrinkage on sintering. Addit Manuf. 2021 Jul 1;43:102007.

[3] Diener S, Zocca A, Günster J. Literature Review: Methods for achieving high powder bed densities in ceramic powder bed based additive manufacturing. Open Ceram. 2021 Sep 27;8:100191.

[4] Mariani M, Frias Blanco G, Mercadelli E, Sánchez-Herencia AJ, Galassi C, Lecis N, et al. Tailoring α-alumina powder morphology through spray drying for cold consolidation by binder jetting. Open Ceram. 2022 Dec 25;12:100307.

[5] Liu J, Lal A, German RM. Densification and shape retention in supersolidus liquid phase sintering. Acta Mater. 1999 Dec 10;47(18):4615–26.

[6] Lecis N, Mariani M, Beltrami R, Emanuelli L, Casati R, Vedani M, et al. Effects of process parameters, debinding and sintering on the microstructure of 316L stainless steel produced by binder jetting. Mater Sci Eng A. 2021 Nov 2;828:142108.

[7] Liu J, Kannan R, Zhang D, Liu T, Nandwana P, Devaraj A. Multi-scale characterization of supersolidus liquid phase sintered H13 tool steel manufactured via binder jet additive manufacturing. Addit Manuf. 2022 Apr 20;56:102834.

[8] Mariani M, Goncharov I, Mariani D, De Gaudenzi G Pietro, Popovich A, Lecis N, et al. Mechanical and microstructural characterization of WC-Co consolidated by binder jetting additive manufacturing. Int J Refract Met Hard Mater. 2021 Nov 1;100:105639.

[9] Lecis N, Beltrami R, Mariani M. Binder jetting 3D printing of 316 stainless steel: Influence of process parameters on microstructural and mechanical properties. Metall Ital. 2021;113(2):31–41.

[10] Mariani M, Beltrami R, Meneghetti F, Azzollini D, Lecis N. Effect of Printing Parameters on the Mechanical Strength of Green Body from Binder Jetting Additive Manufacturing. In: Proceedings - Euro PM2020 Congress and Exhibition. EPMA; 2020.

[11] Baesso I, Karl D, Spitzer A, Gurlo A, Günster J, Zocca A. Characterization of powder flow behavior for additive manufacturing. Addit Manuf. 2021 Nov 13;47:102250.

[12] Bai Y, Wagner G, Williams CB. Effect of Particle Size Distribution on Powder Packing and Sintering in Binder Jetting Additive Manufacturing of Metals. J Manuf Sci Eng. 2017 Aug 1;139(8).

[13] Mariani M, Beltrami R, Brusa P, Galassi C, Ardito R, Lecis N. 3D printing of fine alumina powders by binder jetting. J Eur Ceram Soc. 2021 Aug 8;41(10):5307–15.

[14] Huber D, Vogel L, Fischer A. The effects of sintering temperature and hold time on densification, mechanical properties and microstructural characteristics of binder jet 3D printed 17-4 PH stainless steel. Addit Manuf. 2021 Oct 17;46:102114.

[15] Borujeni SS, Shad A, Venkata KA, Günther N, Ploshikhin V, Sadeghi Borujeni S, et al. Numerical simulation of shrinkage and deformation during sintering in metal binder jetting with experimental validation. Mater Des. 2022 Apr;216:110490.

[16] Mariani M, Mariani D, De Gaudenzi G Pietro, Lecis N. Effect of printing parameters on sintered WC-Co components by binder jetting. Eur J Mater. 2022 Dec 31;2(1):365–80.

[17] Wang F, You S, Jiang D, Ning F. Study on sintering mechanism for extrusion-based additive manufacturing of stainless steel through molecular dynamics simulation. Addit Manuf. 2022 Oct 24;58:102991.

[18] Kannan R, Nandwana P. Predicting sintering window during supersolidus liquid phase sintering of steels using feedstock analysis and CALPHAD. Mater Lett. 2021 Dec 1;304:130648.

[19] Miyata Y, Okugawa M, Koizumi Y, Nakano T. Inverse columnar-equiaxed transition (CET) in 304 and 316l stainless steels melt by electron beam for additive manufacturing (AM). Crystals. 2021 Aug 1;11(8).

Analisi comparative di polveri 316L atomizzate e da riciclo per Binder Jetting

In questo lavoro è analizzata l'idoneità di polveri di acciaio inossidabile 316L da riciclo di scarti metallici per stampa a getto di legante e i risultati sono confrontati con quelli ottenuti da materia prima convenzionale atomizzata a gas. Le principali caratteristiche morfologiche delle particelle, in particolare sfericità e distribuzione dimensionale, sono misurate tramite granulometria ottica e microscopia a scansione elettronica. La portata di rilascio e i parametri di deposizione della stampante sono ottimizzati per ottenere un letto di polvere liscio e omogeneo. In seguito, il letto di stampa è trattato a 180 °C per consolidare i componenti verdi, la cui densità e accuratezza geometrica sono misurate tramite calibro digitale. Infine, le proprietà microstrutturali e meccaniche dei campioni sinterizzati in vuoto sono studiate. La composizione di fase è determinata tramite diffrazione a raggi x e microscopia, con particolare attenzione alla formazione di ferrite δ ai bordi grano. La durezza è valutata tramite micro-indentazione Vickers e confrontata con le proprietà tipiche del 316L da manifattura convenzionale.

PAROLE CHIAVE: BINDER JETTING; ACCIAIO INOSSIDABILE 316L; SINTERIZZAZIONE; AUSTENITE; FERRITE

TORNA ALL'INDICE >